Environmental Science & Technology

pubs.acs.org/est

Article

Open Access

This article is licensed under CC-BY 4.0

# Ionization, Latitude, and Altitude Dependence of Particle Formation in Stratospheric $SO_2$ and $H_2S$ Injection Plumes

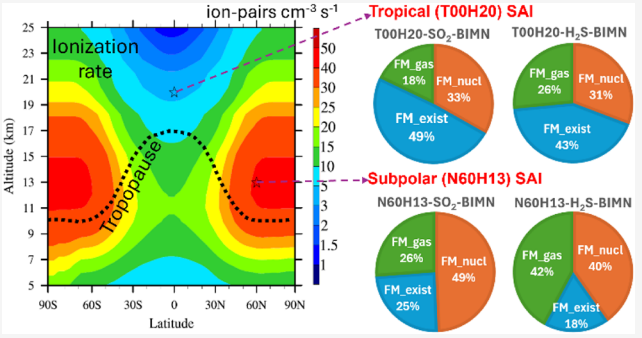
Fangqun Yu*

Cite This: https://doi.org/10.1021/acs.est.6c06576

Read Online

ACCESS | Metrics & More | Article Recommendations | Supporting Information

**ABSTRACT:** Stratospheric aerosol injection (SAI) has received increasing attention as a potential temporary climate intervention strategy. A critical source of uncertainty involves subgrid processes within injection plumes—specifically new particle formation (NPF)—which influence particle size distribution and overall SAI efficacy. This work provides the first comprehensive modeling study of NPF and size distribution evolution within subgrid aircraft plumes at tropical and subpolar sites for both sulfur dioxide ($SO_2$) and hydrogen sulfide ($H_2S$) SAI. Results indicate that $H_2S$ SAI generally produces new particles as effectively as $SO_2$ SAI when the precursor mass injection rate is the same. Notably, due to a much higher ionization rate, subpolar regions exhibit higher particle formation efficiency and less condensation on background aerosols compared to tropical areas. Without considering the ionization effect, NPF in the subpolar $SO_2$ and $H_2S$ SAI plumes is negligible. Furthermore, NPF efficacy diminishes sharply with increasing injection altitude, a trend driven by changing ionization rates and other parameters at higher elevations. The analysis also highlights that particle creation efficiency is strongly affected by other factors. The insights gained contribute to more informed decision-making regarding climate intervention strategies and governance.




**KEYWORDS:** *Stratospheric aerosol injection (SAI), New particle formation, Ion-mediated nucleation, Aerosol size distribution, Subgrid processes*

## INTRODUCTION

Several recent studies suggest that global warming is accelerating,[1,2] which raises concerns about crossing tipping points that could destabilize the climate system. Such destabilization might push the planet toward a hothouse trajectory with potentially irreversible consequences.[3,4] While reducing greenhouse gas emissions must remain a top priority, most climate models indicate that, even if global emissions reach net zero by 2050, global temperatures will likely "overshoot" the 1.5 or 2 °C thresholds established by the Paris Agreement[5,6] and cause significant economic losses.[7] Solar radiation modification (SRM) has gained attention as a temporary measure to mitigate "overshoot" and reduce associated damages,[8−13] despite of potential risks associated with it.[14] Among various SRM techniques, stratospheric aerosol injection (SAI) of sulfur-based compounds is the most extensively studied, mainly because of its well-understood cooling effects and similarities to natural volcanic eruptions.[15] To emulate volcanic activity, most SAI models focus on injecting sulfur dioxide ($SO_2$), although hydrogen sulfide ($H_2S$) has also been proposed due to its lower molecular weight.[14] Direct injection of sulfuric acid ($H_2SO_4$) vapor has been proposed to improve control over particle size distribution and enhance SAI efficacy per unit of sulfur injected.[16] Regarding safety, costs, and feasibility, $H_2S$ and $SO_2$ are considered the most cost-effective and technologically ready options, whereas the limits and technological feasibility of injecting $H_2SO_4$ (and $SO_3$) remain uncertain.[17]

Extensive global modeling studies have confirmed the radiative cooling effects of sulfur-based SAI (e.g., GeoMIP;[18] GLENS;[19] ARISE-SAI;[20]). However, there is a significant spread across models in the predicted radiative forcing efficacy of SAI,[21] which is defined as the globally averaged radiative forcing per unit of sulfur injected. These uncertainties in efficacy and underlying processes hinder the development of sound SAI deployment and governing strategies, making the reduction of these uncertainties a high priority.[10] An additional, yet unaddressed, uncertainty involves subgrid processes within the injection plume, where concentrations of relevant species are vastly higher than background levels, and nonlinear processes influence chemistry and particle size distributions.[22,23] The evolution of the initial plume significantly impacts overall SAI

Received: May 1, 2026
Revised: November 14, 2026
Accepted: November 16, 2026

ACS Publications

© XXXX The Author. Published by American Chemical Society



Downloaded from pubs.acs.org/esthag/article-pdf/doi/10.1021/acs.est.6c06576/6928922O/acs.est.6c06576.pdf by guest on 28 November 2026

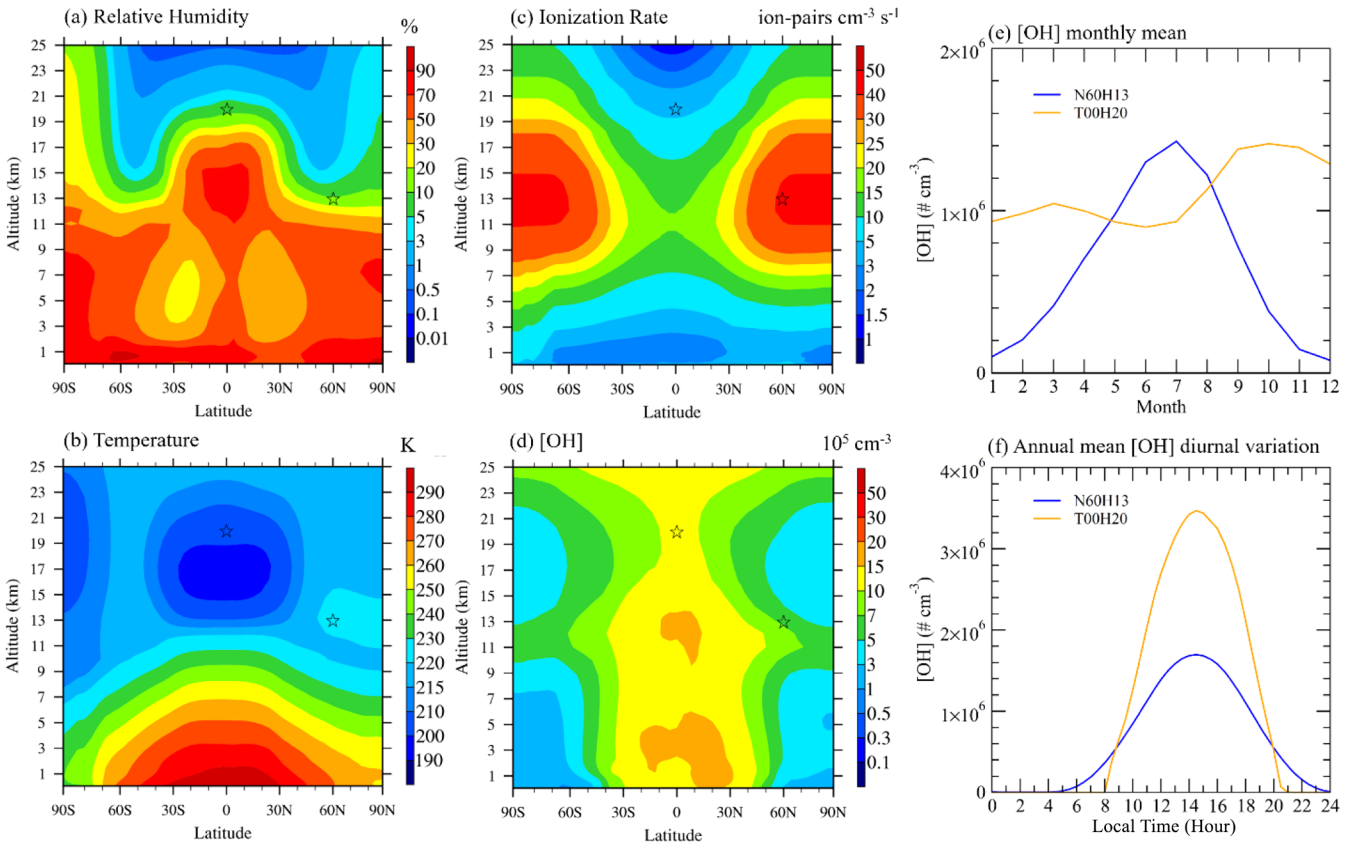



**Figure 1.** Multiple-year (2011−2017) mean zonal distributions of (a) relative humidity (RH), (b) temperature (T), (c) ionization rate (Q), and (d) hydroxyl radical (OH) concentration ([OH]) from GEOS-Chem-APM simulations. (e) and (f) presents seasonal and diurnal variations of [OH] at two selected SAI injection sites at latitude and altitude of 0° and 20 km (T00H20), and 60°N and 13 km (N60H13) marked on (a−d). Both sites are assumed to be at longitude of 70°W.

effectiveness, as it influences the final aerosol particle size distribution.[16,24]

The importance of understanding plume-scale processes has been emphasized in several reports, including the 2021 National Academies of Sciences, Engineering, and Medicine (NASEM) report.[10] One of the key research priorities identified is to address critical knowledge gaps regarding the evolution of aerosol particle size distribution within subgrid plumes—specifically, plume dynamics, particle nucleation, growth, and how deployment choices influence outcomes.[10] The Geoengineering Modeling Research Consortium highlighted the need to improve the representation of plume-scale aerosol microphysical processes in global models.[25] Based on the relative importance of various uncertainties, the Reflective Scientific Advisory Board (SAB) recommended three research priorities: reducing uncertainties related to aerosol size distribution and small-scale physics, developing observation techniques for plumes and deployment strategies, and addressing engineering challenges for initial delivery systems.[26] Understanding plume microphysics is central to these priorities, as it informs dispersal mechanisms, safety considerations, and cost assessments for materials and aircraft-based deployment.[17]

Research on aerosol microphysics in SAI plumes remains limited. While some studies have examined particle formation and size evolution in $H_2SO_4$ vapor injection,[16,27,28] comparable research on aircraft-based $SO_2$ and $H_2S$ plumes is scarce or nonexistent. This study represents the first comprehensive investigation into new particle formation (NPF) and particle size distribution evolution in subgrid aircraft-based plumes for both $H_2S$ and $SO_2$ at two different sites (one tropical and one subpolar), using a state-of-the-art advanced particle microphysics model that has previously been employed to study the formation and evolution of particles and contrails in aircraft plumes.[28−31] Alongside the tropical site, we selected a subpolar site for a detailed plume-scale study, reflecting increased interest in High-Latitude Low-Altitude SAI.[32−36]

## RESULTS AND DISCUSSIONS

For $H_2S$ and $SO_2$ SAI, it is essential to understand the oxidation of gaseous species, formation and growth of new particles, and whether there is any significant scavenging of precursors and newly formed particles by pre-existing particles in the subgrid plume. The oxidation of $SO_2$ or $H_2S$ and formation of new particles occur gradually and depend strongly on ambient conditions. To model these processes as realistically as possible, key parameters are derived from the GEOS-Chem-APM model (see Methods). Figure 1 illustrates the multiyear mean zonal distributions of relative humidity (RH), temperature (T), ionization rate (Q), and hydroxyl radical concentration ([OH]). It also depicts seasonal and diurnal variations of [OH] at two representative injection sites: a tropical site at 0° latitude at 20 km altitude (T00H20) and a subpolar site at 60°N at 13 km altitude (N60H13). Both sites are assumed to be at longitude of 70°W. The baseline altitude for each site is approximately 3 km above the respective tropopause. Due to the roughly symmetric distribution of key parameters in the stratosphere, results at the 60°N site are applicable to the corresponding southern hemisphere locations at 60°S. The

Downloaded from pubs.acs.org/esthag/article-pdf/doi/10.1021/acs.est.6c06576/6289220/acs.est.6c06576.pdf by guest on 28 November 2026


https://doi.org/10.1021/acs.est.6c06576
Environ. Sci. Technol. XXXX, XXX, XXX−XXX

parameters for baseline and sensitivity analyses are summarized in Table 1 and described in Methods. Ref 33 showed that high-latitude SAI can be more effective if injection is limited to spring, i.e., March-April-May (MAM) in the Northern Hemisphere. Therefore, spring (MAM) mean values of [OH], T, and RH are used for the subpolar-site baseline case, whereas annual means of these variables are used for the tropical site. The baseline simulation uses binary ion-mediated nucleation (BIMN) involving $H_2SO_4$–$H_2O$ binary ions, and a sensitivity analysis considers kinetic binary homogeneous nucleation (KBHN) to evaluate the role of ionization. As shown in ref 37, both BIMN and KBHN schemes agree well with CLOUD laboratory experiments conducted at stratospheric temperatures[38,39] and BIMN aligns well with field measurements of aerosol number concentrations in the lowermost stratosphere.[40]

**Table 1. Parameters for Baseline and Sensitivity Cases in Aircraft-Based SAI of $SO_2$ and $H_2S$**

| Parameter | Baseline | Sensitivity study range |
|---|---|---|
| MIR (kgX/s, X = $SO_2$, $H_2S$) | 25 | 1–100 |
| Dilution exponent coefficient ($\gamma$) | 1.25 | 0.5–2.0 |
| $S_B$ ($\mu m^2/cm^3$) | 5 | 1–30 |
| Ambient $SO_2$ (ppt) | 100 | 1–1000 |
| [OH] Seasonal variation | Annual mean for T00H20 and spring (MAM) mean for N60H13 | [OH] in month 1–12 |
| Injection height (H) | 3 km above tropopause | 1–11 km above tropopause |

Figure 2 presents a simulated 30-day evolution of plume gases and particle properties for both $SO_2$ and $H_2S$ SAI at T00H20 under the baseline case, considering (BIMN) and without (KBHN) ionization effect on NPF. With SAI material injection rate (MIR) of 25 kgX/s (X = $H_2S$, $SO_2$), $[SO_2]$ and $[H_2S]$ in the initial plume are very high, reaching $1.73 \times 10^{17}$ $cm^{-3}$ and $3.26 \times 10^{17}$ $cm^{-3}$, respectively. At the same MIR, $[H_2S]$ is 1.88 times higher than $[SO_2]$ due to difference in molecular weight. At time zero, as a result of sulfur in the fuel and an assumed 3% of fuel sulfur converted to $H_2SO_4$, $[H_2SO_4]$ is $3.82 \times 10^{11}$ $cm^{-3}$ for both SAI cases and $[SO_2]$ is $1.24 \times 10^{13}$ $cm^{-3}$ for $H_2S$ SAI. The presence of high $[H_2SO_4]$ from fuel sulfur leads to the formation of volatile particles of 1–5 nm in the fresh exhaust plume, based on both BIMN (Figure 2a2, b2) and KBHN (Figure 2a3, b3) schemes. In BIMN, the impact of chemiions[29] is considered, resulting in particles formed on chemiions being slightly larger, although the neutral mode formed via KBHN dominates the number concentrations. Higher fuel sulfur content or direct coinjection of $H_2SO_4$ can enhance NPF shortly after emissions. However, the impact of these particles diminishes quickly as the plume further dilutes, unless $H_2SO_4$ from fuel sulfur or coinjection are substantial and comparable to injected SAI materials. Under conditions assumed in this study, $H_2SO_4$ oxidized from injected $SO_2$ or $H_2S$ dominates particle formation, growth, and mass.

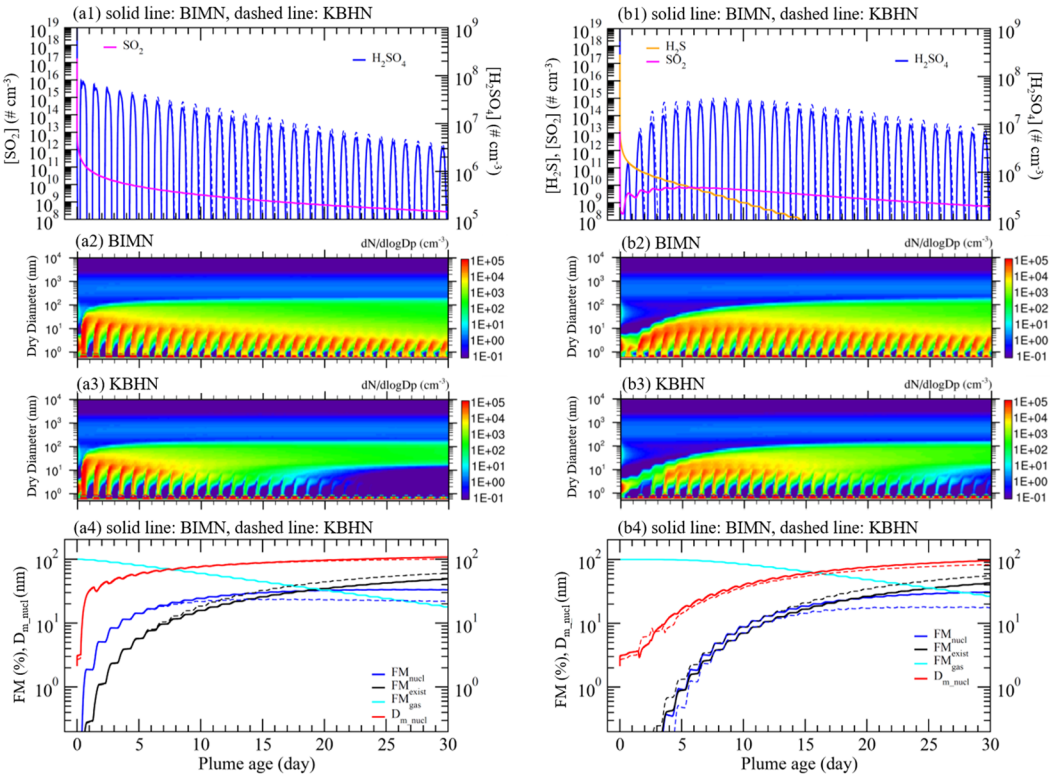



**Figure 2.** 30-day time evolution of selected variables and particle size distributions in exhaust plumes with $SO_2$ (left column, a1–a4) and $H_2S$ (right column, b1–b4) SAI at T00H20 under baseline case with two nucleation schemes (BIMN and KBHN). (a1, b1) concentrations of $SO_2$ ($[SO_2]$), $H_2S$ ($[H_2S]$), and sulfuric acid vapor ($[H_2SO_4]$) (dashed line is for KBHN); (a2, b2) particle number size distribution (PNSD) based on BIMN; (a3, b3) PNSD based on KBHN; and (a4, b4) fraction of injected sulfur (S) mass ended up in newly nucleated particles ($FM_{nucl}$), pre-existing particles ($FM_{exist}$), and gases ($H_2S$ + $SO_2$) ($FM_{gas}$); and mass-weighted mean diameter of newly nucleated particles (>3 nm) ($D_{m_nucl}$). The baseline case, as specified in Table 1, assumes the background stratosphere already with some SAI.

Downloaded from pubs.acs.org/esthag/article-pdf/doi/10.1021/acs.est.6c06576/6928220/acs.est.6c06576.pdf by guest on 28 November 2026


https://doi.org/10.1021/acs.est.6c06576
Environ. Sci. Technol. XXXX, XXX, XXX–XXX

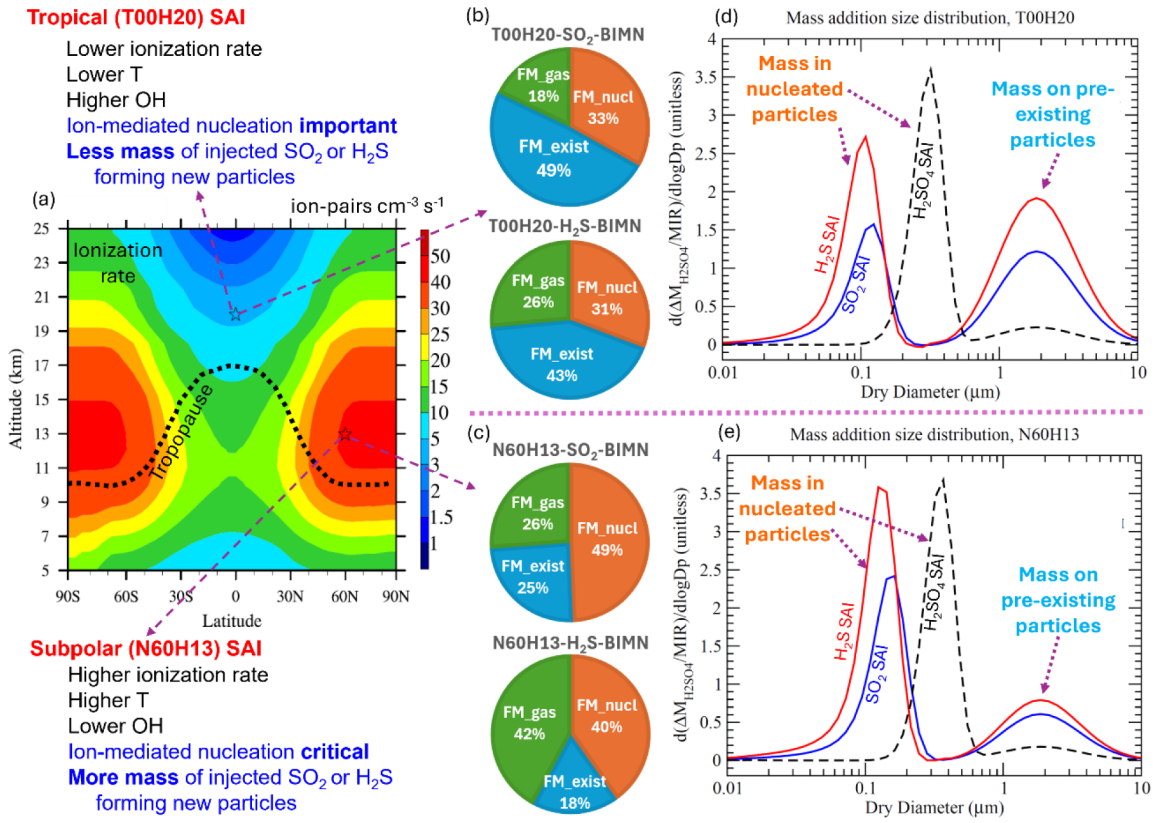



**Figure 3.** Tropical-subpolar differences in the distributions of injected sulfur at the end of day 30 in the $SO_2$ and $H_2S$ SAI plumes under baseline conditions. (a) Zonally averaged ionization rates and locations of two example sites (tropical T00H20 and subpolar N60H13) and the tropopause; (b-c) fraction of injected sulfur mass in newly nucleated particles ($FM_{nucl}$), pre-existing particles ($FM_{exist}$), and gases ($H_2S + SO_2$) ($FM_{gas}$); and (d–e) size distributions of condensed $H_2SO_4$ mass addition per flight time normalized to MIR: $d(\Delta M_{H2SO4}/MIR)/d\,logDp$ at the two sites for $H_2S$ (red line) and $SO_2$ (blue line) SAI, with corresponding $H_2SO_4$ SAI (black dashed line) added for comparison.

Ionization, which is ubiquitous in the atmosphere, is known to enhance the formation and growth of nanometer particles through solid physical mechanisms and has been shown to be significant in generating new particles in the lower stratosphere.[37] BIMN is limited by the ionization rate, and under certain conditions, KBHN can become dominant. The relative importance of ionization can be inferred from the differences between BIMN and KBHN simulations. At T00H20, due to very cold temperatures ($T$ < 210 K, Figure 1b) and low ionization rate (Figure 1c), KBHN dominates when $[H_2SO_4]$ exceeds approximately $3 \times 10^7$ $cm^{-3}$ but becomes negligible when $[H_2SO_4]$ is below about $7 \times 10^6$ $cm^{-3}$. BIMN dominates NPF when $[H_2SO_4]$ is below ~$3 \times 10^7$ $cm^{-3}$ and is important after ~day 5 in $SO_2$ SAI (Figure 2a2, a3) and throughout all days for $H_2S$ SAI (Figure 2b2, b3). When BIMN is dominant or important, $[H_2SO_4]$ is slightly higher in the KBHN case (Figure 2a1, b1, comparing solid and dashed lines) because fewer new particles are formed, leading to a reduced condensation sink.

$H_2S$ has a typical lifetime of several days in the lower stratosphere, as evidenced by the decrease in $[H_2S]$ and the increase in $[SO_2]$ during the first several days of plume age (Figure 2b1). During this initial period, $[SO_2]$ and $[H_2SO_4]$ levels, and consequently the potential for new particle formation and growth in $H_2S$ SAI (Figure 2b1–3), are much lower or weaker than those observed in $SO_2$ SAI (Figure 2a1–3). For $SO_2$ SAI, mass-weighted mean diameter of newly nucleated particles ($D_{m_nucl}$) increases rapidly (Figure 2a4) within the first few days, with some particles already growing to approximately 100 nm (Figure 2a2). Conversely, for $H_2S$ SAI, nucleation and growth rates gradually increase as $[SO_2]$ and $[H_2SO_4]$ levels rise, peaking around days 7–10. Interestingly, after about day 5, $[SO_2]$ and $[H_2SO_4]$ levels—and thus nucleation rates—for $H_2S$ SAI become higher than those for $SO_2$ SAI. This is attributable to the initial $[H_2S]$ being 1.88 times higher than $[SO_2]$ under the same MIR. After a month (day 30), both $SO_2$ SAI and $H_2S$ SAI exhibit similar $D_{m_nucl}$ (~100 nm) and fraction of injected sulfur ending on nucleated particles ($FM_{nucl}$) (~30% for BIMN and ~20% for KBHN), despite $H_2S$ SAI injecting 88% more sulfur at the same MIR. It should be noted that the size of newly nucleated aerosols on day 30 is not representative of the actual size of SAI-produced aerosols, considering (1) these particles are expected to continue to grow during their lifetime of up to 1–2 years in the stratosphere and (2) a large fraction of injected sulfur may end up on pre-existing aerosols. To obtain representative sizes of SAI-produced particles, multiple-year global model simulations with size-resolved particle microphysics and proper representation of subgrid plume scale processes are needed.

The fraction of injected sulfur ending on pre-existing particles in background air ($FM_{exist}$) is approximately 5% higher for $SO_2$ SAI (BIMN 49%, KBHN 61%) than for $H_2S$ SAI (BIMN 43%, KBHN 56%), while the remaining sulfur on gases is about 8% higher for $H_2S$ SAI (26%) versus $SO_2$ SAI (18%). These differences stem from variations in initial concentrations, oxidation pathways, and microphysical processes, emphasizing the importance of understanding the controlling factors and their nonlinear dependencies.

Downloaded from pubs.acs.org/esthag/article-pdf/doi/10.1021/acs.est.6c06576/6928920/acs.est.6c06576.pdf by guest on 28 November 2026


https://doi.org/10.1021/acs.est.6c06576
Environ. Sci. Technol. XXXX, XXX, XXX−XXX

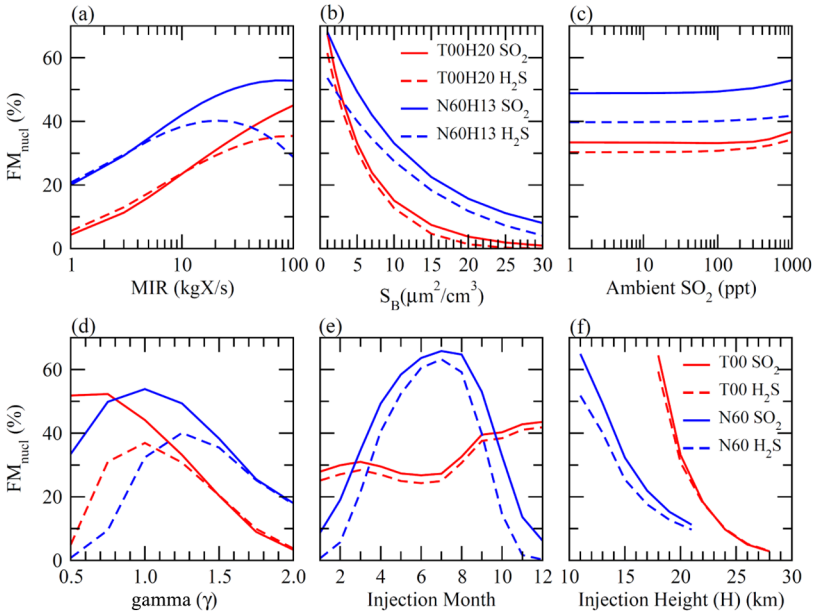



**Figure 4.** Dependence of $FM_{nucl}$ at end of day 30 on (a) MIR, (b) surface area of pre-existing particles in the background stratosphere ($S_B$), (c) ambient $SO_2$ concentration, (d) dilution exponent coefficient ($\gamma$), (e) injection month, and (f) injection height (H) for both $SO_2$ (solid lines) and $H_2S$ (dashed lines) SAI at two sites (red: tropical site T00H20; blue: subpolar site N60H13).

Compared to the tropical injection site T00H20 (Figure 2), particle formation and evolution at the subpolar site N60H13 (Supplementary Figure S1) and the distributions of injected sulfur at the end of day 30 (Figure 3) display notable differences. First, the initial number concentration of injected species is higher by a factor of 2.8 (Figures S1a1, S1b1), owing to lower initial volume associated with higher atmospheric pressure and air density (a result of ideal gas law). Consequently, the average $[H_2SO_4]$ is slightly elevated despite lower [OH] (Figure 1f). Second, the injected species have a longer lifetime at the subpolar site due to lower [OH] and a larger fraction remains as gases at day 30 (26% for $SO_2$ SAI and 42% for $H_2S$ SAI) (Figures 3c, S1a4, S1b4). Third, BIMN dominates the nucleation process, with KBHN being negligible except during the initial minutes when particles form from $H_2SO_4$ derived from fuel sulfur (Figures S1a2-a3, S1b2-b3). The higher ionization rate (Figures 1c, 3a) enhances BIMN, while the higher temperature (Figure 1b) inhibits KBHN at the subpolar site. Therefore, considering ionization effects is critical for high-latitude, subpolar injections, a factor not previously emphasized in studies. Fourth, at the subpolar site, $FM_{nucl}$ is higher (49% vs 33% for $SO_2$ SAI, 40% vs 31% for $H_2S$ SAI), while $FM_{exist}$ is significantly lower (25% vs 49% for $SO_2$ SAI, 18% vs 43% for $H_2S$ SAI) based on BIMN (Figure 3b−c). This higher $FM_{nucl}$ and lower $FM_{exist}$ at the high-latitude site are somewhat counterintuitive, as one might expect more effective particle formation at the tropical site due to stronger photochemistry and lower temperatures. Our analysis indicates that the elevated $FM_{nucl}$ and reduced $FM_{exist}$ at N60H13 (compared to T00H20) are primarily driven by a 10-fold increase in ionization rate (Figure 3a), which substantially enhances nucleation and growth processes (comparing Figures S1a2, S1b2 with Figure 2a2, b2). This underscores the importance of accounting for ionization effects and their spatial variability in SAI modeling. The diurnal variations of $FM_{nucl}$ in KBHN cases are linked to diurnal fluctuations in $[H_2SO_4]$ and its clusters, which are treated as part of the nucleated particles. Finally, $D_{m_nucl}$ is 29% larger for $SO_2$ SAI (139 nm vs 108 nm) and 23% larger for $H_2S$ SAI (119 nm vs 97 nm) at the subpolar site when ionization effects are included (Figures 3d−e, S1a4, S1b4, 2a4, b4).

To further illustrate the tropical-subpolar contrast in the distribution of the condensed portion of injected sulfur (i.e., $FM_{nucl} + FM_{exist}$), Figure 3d−e presents the size distributions of $H_2SO_4$ mass addition to particles ($\Delta M_{H2SO4}$ = total mass − background mass) per injection time normalized to MIR (i.e., $d(\Delta M_{H2SO4}/MIR)/d \log D_p$) at the end of day 30 in the baseline $SO_2$ and $H_2S$ SAI plumes. For comparison, the corresponding size distributions for $H_2SO_4$ SAI are also given. Compared to previous simulations reported in ref 28, the $H_2SO_4$ SAI simulations given here assume aircraft configurations as described in Methods M2 and baseline conditions specified in Table 1 except with X = $H_2SO_4$. Figure 3d−e shows that, despite a substantial fraction of injected $SO_2$ or $H_2S$ not yet being oxidized at day 30, the total $H_2SO_4$ mass that has already ended up on particles (both nucleated and pre-existing) is highest for $H_2S$ and lowest for $H_2SO_4$ SAI. This is not surprising because, with the same MIR, $SO_2$ SAI injects 53% more and $H_2S$ 188% more sulfur (S) than $H_2SO_4$ SAI. It can be clearly seen from Figure 3d−e that the fraction of mass forming new particles is higher at the subpolar site than that at the tropical site, for both $SO_2$ and $H_2S$ SAI. As pointed out in previous publications,[16,28] most of the mass in $H_2SO_4$ SAI forms new particles with sizes depending on injection and mixing rates. At the baseline MIR of 25 kg/s, $H_2S$, $SO_2$, and $H_2SO_4$ SAI produce new particles with $D_{m_nucl}$ of 97, 108, and 306 nm at the tropical site and 119, 139, and 345 nm at the subpolar site, respectively. Since these nucleated particles will continue to grow, the optimum initial sizes for maximum SAI efficacy depend on SAI strategies (tropical annual versus polar springtime injections, injection locations and altitudes, etc.) and particle residence time in the stratosphere. While the sizes of initial particles in the subgrid plumes can be optimized by controlling MIR when other parameters are known, global model simulations with proper

Downloaded from pubs.acs.org/esthag/article-pdf/doi/10.1021/acs.est.6c06576/6928922O/acs.est.6c06576.pdf by guest on 28 November 2026


https://doi.org/10.1021/acs.est.6c06576
Environ. Sci. Technol. XXXX, XXX, XXX−XXX

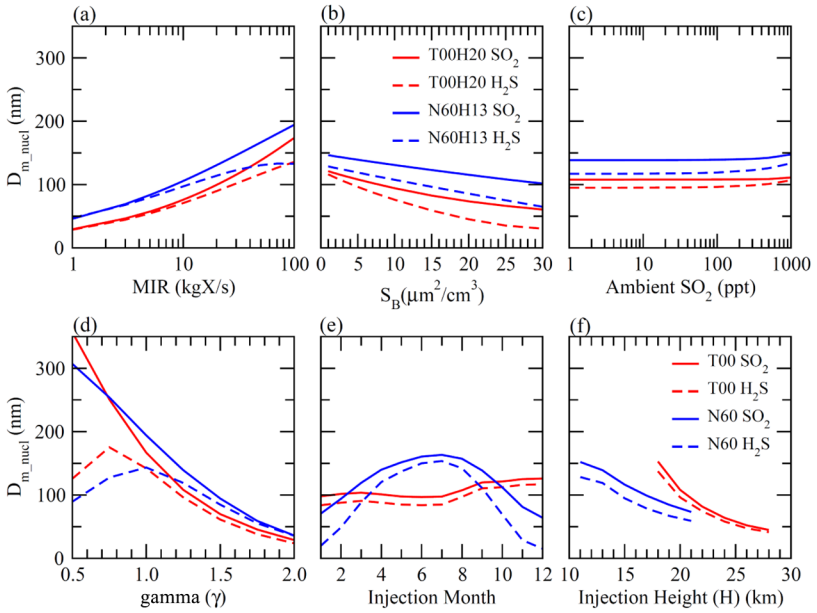



**Figure 5.** Same as Figure 4 except for $D_{m_nucl}$.

subgrid scale parametrizations are needed to determine optimum SAI strategies.

Many factors influence the formation and evolution of new particles in $SO_2$ and $H_2S$ SAI plumes. We conducted sensitivity analyses based on key parameters and their ranges specified in Table 1, with ionization effects included in all simulations. Figures 4 and 5 depict the dependence of $FM_{nucl}$ and $D_{m_nucl}$ at day 30 on these parameters for both $SO_2$ and $H_2S$ SAI at the tropical (T00H20) and subpolar (N60H13) sites. In each panel, baseline values of other parameters are assumed, except for the variable on the *x*-axis.

$FM_{nucl}$ (Figure 4a) and $D_{m_nucl}$ (Figure 5a) generally increase with increasing MIR, except for $H_2S$ SAI at N60H13. The increase is more pronounced at the tropical site and at lower MIR values. This trend results from the interplay between photochemistry and aerosol microphysics. For $SO_2$ SAI, higher MIR favors the generation of more and larger nucleated particles, especially at the tropical site. The nonlinear relationship of $FM_{nucl}$ with MIR for $H_2S$ SAI at the subpolar site suggests an optimal MIR exists. Notably, at MIR < 30 kgX/s, $FM_{nucl}$ at N60H13 is consistently higher than that at T00H20, reaching up to a factor of 5 for $SO_2$ SAI (from 4.3% to 21.6% at MIR = 1 kgX/s) and a factor of 4 for $H_2S$ SAI (from 5.5% to 21.5% at MIR = 1 kgX/s). These results imply that subpolar $SO_2$ and $H_2S$ SAI may be more effective in producing new particles rather than merely enlarging pre-existing particles, primarily due to the higher ionization rates at high latitudes. As MIR increases from 1 kgX/s to 100 kgX/s, $D_{m_nucl}$ increases from 25 to 50 nm to 110−180 nm (Figure 5a). Interestingly, at low MIR (<∼10 kgX/s), $FM_{nucl}$ and $D_{m_nucl}$ for $H_2S$ SAI are comparable to those for $SO_2$ SAI, allowing for a higher absolute number of new particles because $H_2S$ can carry 88% more sulfur at the same MIR. At higher MIR, the advantage diminishes as the difference in $FM_{nucl}$ widens.

Without volcanic activity, the surface area of pre-existing particles in background stratosphere ($S_B$) at ∼3 km above the tropopause varies from about 1 $\mu m^2/cm^3$ in tropical regions to about 3 $\mu m^2/cm^3$ in polar regions. SAI can significantly increase $S_B$, reaching approximately 10 $\mu m^2/cm^3$ with an injection of 1 teragram of sulfur per year.[21] $S_B$ is expected to increase as SAI deployment is scaled up and our study indicates that $S_B$ significantly impacts $FM_{nucl}$ (Figure 4b) and $D_{m_nucl}$ (Figure 5b). Elevated $S_B$ inhibits new particle formation and growth due to increased scavenging and consumption of $H_2SO_4$ from oxidation of $H_2S$ and $SO_2$. At T00H20 for $SO_2$ and $H_2S$ SAI respectively, $FM_{nucl}$ decreases from 67.6% and 61.4% at $S_B$ of 1 $\mu m^2/cm^3$ to 15.1% and 12.7% at 10 $\mu m^2/cm^3$, and to 0.9% and 0.04% at 30 $\mu m^2/cm^3$. Similarly, at N60H13, $FM_{nucl}$ drops from 65.4% and 47.6% at 1 $\mu m^2/cm^3$ to 32.4% and 24.5% at 10 $\mu m^2/cm^3$, and to 7.7% and 3.5% at 30 $\mu m^2/cm^3$. Increasing $S_B$ from 1 to 10 and then 30 $\mu m^2/cm^3$ reduces $D_{m_nucl}$ from 116 to 142 nm to 76−126 nm, and further down to 30−97 nm. Overall, the tropical site (T00H20) exhibits lower $FM_{nucl}$ and smaller $D_{m_nucl}$, indicating higher efficiency of new particle generation at the subpolar site. The nonlinear and fast decrease of $FM_{nucl}$ and $D_{m_nucl}$ may imply that, as SAI deployment progresses and SAI aerosols accumulate, the efficacy of $H_2S$ and $SO_2$ SAI in generating new particles of optimized sizes decreases.

Ambient $[SO_2]$ within the investigated range (1−1000 ppt) has the least impact on $FM_{nucl}$ and $D_{m_nucl}$. As shown in Figures 4c and 5c, both parameters increase slightly only when ambient $[SO_2]$ exceeds approximately 500 ppt. The dilution exponent coefficient ($\gamma$) has a strong, nonlinear influence on both $FM_{nucl}$ and $D_{m_nucl}$ (Figures 4d, 5d). As $\gamma$ increases, $FM_{nucl}$ initially rises, reaching a maximum of about 50% (for $SO_2$ SAI), then declines to below 5% (at T00H20). $D_{m_nucl}$ for $H_2S$ SAI first increases and then decreases with increasing $\gamma$, while for $SO_2$ SAI, it decreases monotonically from 280 to 360 nm at $\gamma$ = 0.5 to approximately 30 nm at $\gamma$ = 2.0. This high sensitivity underscores the necessity of accurately quantifying mixing processes to improve predictions and optimize SAI outcomes. Variations in $\gamma$ are expected to be significant in the lower stratosphere due to changes in wind shear and turbulence, emphasizing the importance of incorporating such variability into subgrid parametrizations.

Figures 4e and 5e illustrate the influence of the injection month, which affects [OH] levels (Figure 1e). Seasonal variations in $FM_{nucl}$ and $D_{m_nucl}$ generally follow those of [OH], highlighting the importance of accurately characterizing

Downloaded from pubs.acs.org/esthag/article-pdf/doi/10.1021/acs.est.6c06576/6289220/acs.est.6c06576.pdf by guest on 28 November 2026


https://doi.org/10.1021/acs.est.6c06576
Environ. Sci. Technol. XXXX, XXX, XXX−XXX

[OH] and its temporal fluctuations. Subpolar low-altitude SAI during spring has been proposed to reduce surface temperatures and preserve ice.[32−34] Notably, during April-May at N60H13, $FM_{nucl}$ and $D_{m_nucl}$ are significantly higher than at the tropical site T00H20 for both $SO_2$ and $H_2S$ SAI, indicating that low-altitude subpolar injections can be potentially effective. Future work should explore how this difference in subgrid plume-scale new particle formation efficacy affects the forcing efficiency contrast between high-latitude low-altitude and low-latitude high-altitude $SO_2$ (and $H_2S$) SAI.[35,36] An additional key finding is that both $FM_{nucl}$ and $D_{m_nucl}$ decrease rapidly as the injection height ($H$) increases for both $SO_2$ and $H_2S$ SAI at tropical and subpolar regions (Figures 4f, 5f). This rapid decline is primarily due to the decrease in ionization rate (Figure 1c), relative humidity (Figure 1a), and air density with increasing height. The increase in ambient temperature at T00H20 and decrease in [OH] at N60H13 with increasing height also contributed to the decline. While high injection height is generally considered to prolong aerosol residence time in the stratosphere and enhance SAI efficacy,[36] this study suggests that previous studies may overestimate this effect and thus warrant re evaluation. In such a case, robust nucleation scheme(s) that correctly capture the dependence of particle formation rates on relevant variables are essential.

The present study is subject to uncertainties including the ion-mediated and neutral nucleation thermodynamics under stratospheric conditions, inhomogeneous mixing and detailed chemistry in the subgrid plumes, dilution rates, and properties of ambient air mixing into the plume. The critical role of ionization in enhancing new particle formation in $SO_2$ and $H_2S$ SAI plumes, as shown in this study, needs to be confirmed with field measurements. To have more informed decision-making regarding SAI strategies and governance, further laboratory and field measurements are essential to constrain various processes (nucleation schemes, chemistry, mixing, etc.) and evaluate the performance of aerosol microphysics models under various stratospheric conditions. Further research is also needed to understand how the new insights revealed in this study translate to final outcomes of SAI, which depends on injection scenarios, parametrization of subgrid processes, and representations of aerosols in global models.

## METHODS

### M1: Comprehensive Advanced Particle Microphysics (C-APM) Model

The advanced particle microphysics (APM) model was developed in the late 1990s to investigate the formation and evolution of aerosols and contrails within aircraft plumes.[29,30] This model adapted some algorithms and structural elements from a sectional aerosol microphysics model initially developed by Turco and colleagues for studying stratospheric aerosols[41] and later modified to simulate tropospheric particles.[42] The APM model features new algorithms and physics, including a hybrid bin structure, adjustable size ranges and bin resolution, multiple aerosol types, explicit treatment of kinetic nucleation starting from molecular scales, consideration of ionization and charge effects, and modularized microphysics subroutines. Over the past decades, the model has undergone continuous development and improvement, resulting in two distinct versions: a comprehensive APM (C-APM) for detailed aerosol microphysics that accounts for kinetic nucleation and charge effects constrained by laboratory data and quantum chemistry calculations (ref 28 and the references therein), and a simplified, computationally efficient version (APM) optimized for three-dimensional size-resolved aerosol simulations (ref 21 and the references therein).

The current study employs an updated configuration of the C-APM, tailored for aircraft plume applications as detailed in ref 28 and ref 31. A simplified sulfur chemistry scheme is integrated to model sulfur species oxidation within the plume. The model explicitly solves interactions among ions, neutral and charged clusters of various sizes, vapor molecules, and pre-existing particles, thereby overcoming limitations of classical nucleation models in aircraft wake applications.[28] It employs a sectional bin structure to represent particle sizes, ranging from a single $H_2SO_4$ molecule to particles measuring tens of micrometers in diameter. A total of 112 bins cover a size spectrum from 0.54 nm to 41.6 $\mu$m. The model considers three aerosol types: nucleated sulfuric acid particles, soot particles from incomplete jet fuel combustion, and background aerosols. In the presence of chemiions and ambient ionization, sulfuric acid particles are further categorized into neutral, positively charged, and negatively charged clusters or particles. The model tracks separately the scavenging of sulfuric acid vapor by soot and background particles through direct condensation and coagulation processes.

### M2: Aircraft-Based SAI Platform, Injection Rate, and Plume Dilution

Aircraft are considered a practical and advantageous platform for SAI due to their cost-effectiveness, payload capacity, maneuverability, and compatibility with existing aviation infrastructure.[43,44] Alternative concepts such as balloons, tethered pipes, guns, or rockets have been proposed, but current aircraft technology offers a more feasible approach. For effective global SAI, especially in the tropics and subtropics' lower stratosphere above the tropopause, deployment would require specially designed high-altitude aircraft.[43,45] In the subpolar regions, where the tropopause is lower, existing large jets could potentially be used for injection materials into the stratosphere.[34]

Key parameters for the aircraft platform include flight speed, fuel consumption rate, payload capacity for SAI materials, injection rate, and plume dilution ratio. This study adopts the design specifications of a conceptual first-generation SAI aircraft, the SAIL-1, as described in refs [44−46]. SAIL-1 has a weight comparable to a large narrow-body passenger aircraft such as the Airbus A321, with a fuel consumption rate of approximately 1.84 kg/s.[44] Operating at an altitude of 20 km, it can cruise at Mach 0.55 to Mach 0.92 (0.16 km/s to 0.27 km/s).[45] The aircraft's payload capacity is 15.7 tons, with a typical cruise duration of about 10 min, enabling an injection rate of roughly 25 kg/s of SAI material.[46] In this study, the baseline SAI material injection rate (MIR) is set at 25 kgX/s (where X represents $SO_2$ or $H_2S$), with sensitivity analyses spanning from 1 to 100 kgX/s. The aircraft's cruise speed is assumed to be 0.25 km/s (~0.8 Mach) and fuel consumption at 1.84 kg/s. The fuel's sulfur content is assumed to be 500 ppm, with 3% of sulfur oxidized into $H_2SO_4$ during combustion and the remaining emitted as $SO_2$.[31] The emission index of soot particles from fuel combustion is based on typical jet engine measurements, with size distributions derived from ground-based data.[47]

It is assumed that $SO_2$ and $H_2S$ are injected as gases, entrained into the aircraft wake plume. The dilution of the plume over a few hours is parametrized following ref 48:

$$DR = 7000(t/t_1)^{0.8} \quad (1)$$

where $t_1 = 1$ s, and $0.006\ \text{s} \le t \le 10^4$ s

Here, $t$ is the plume age in seconds, and $DR$ is the dilution ratio, defined as the ratio of the mass of gases in the plume to the mass of fuel burned per unit flight distance ($m_{fuel}$, kg-fuel km$^{-1}$). This parametrization was derived from over 70 plume encounters in the upper troposphere and lower stratosphere, covering ages from milliseconds to 5700 s.[48] For plume ages exceeding $10^4$ seconds, the dispersion is approximated as[49]

$$DR = DR_2(t/t_2)^{\gamma} \quad (2)$$

where $t_2 = 10^4$ s, and $t \ge 10^4$ s.

In this equation, $DR_2$ is the dilution ratio at $t = t_2$, and $\gamma$ is the dilution exponent coefficient, which depends on atmospheric turbulence, diffusivity, and wind shear.[49] According to eq 9 given in ref 49, increased wind shear shifts the dependence of $DR$ on plume age from a

Downloaded from pubs.acs.org/esthag/article-pdf/doi/10.1021/acs.est.6c06576/6928922O/acs.est.6c06576.pdf by guest on 28 November 2026


https://doi.org/10.1021/acs.est.6c06576
Environ. Sci. Technol. XXXX, XXX, XXX−XXX

square root ($\gamma = 0.5$) to linear ($\gamma = 1.0$), and eventually to quadratic ($\gamma = 2.0$). In this study, the baseline value of $\gamma$ is set at 1.25, with sensitivity analyses ranging from 0.5 to 2.0.

The cross-sectional area of the plume ($A$) is calculated as

$$A = (DR \times (m_{fuel} + MIR))/\rho \quad (3)$$

where $\rho$ is the air density within the plume, and MIR accounts for the contribution of injected material to the plume volume, which is generally minimal after vortex formation. This simplified parametrization assumes uniform mixing across the plume cross-section, representing average conditions within the SAI plume. The simulation begins at $t = t_0 = 0.006$ s. The concentration of injected species X ([X], where X = $SO_2$ or $H_2S$) at this initial time is computed as

$$[X] = MIR \times N_A/(M_X \times A_0) \quad (4)$$

where $N_A$ is Avogadro's number, $M_X$ is the molecular weight of species X, and $A_0$ is the effective plume cross-sectional area at $t_0$.

### M3: Ambient Conditions, Injection Location, and Oxidation Parameterization

Unlike the rapid gas-to-particle conversion in $H_2SO_4$ vapor SAI plumes,[28] the oxidation of $SO_2$ or $H_2S$ occurs gradually via OH reactions, which depend strongly on location and time. To be as realistic as possible, [OH] and other relevant parameters (Figure 1) are derived from the GEOS-Chem model,[50] a state-of-the-art global chemistry transport model with a tropospheric−stratospheric chemistry extension,[51] coupled with the sectional APM model.[37] GEOS-Chem is driven by meteorological data from the Goddard Earth Observing System (GEOS), and its performance in simulating particles in the lower stratosphere has been validated against in situ observations from the Atmospheric Tomography Mission (ATom).[37]

In the background lower stratosphere, [OH] is mainly governed by a rapid photochemical cycle influenced by solar UV radiation, water vapor, and ozone levels. The balance between production from excited-state oxygen atoms and loss through reactions with nitrogen oxides ($NO_y$) and hydroperoxyl radicals ($HO_2$) determines the overall OH abundance, which exhibits significant spatial, seasonal, and diurnal variability.[52] In the present study, the [OH] variations at the selected sites are derived from GEOS-Chem simulations (Figure 1e−f). The oxidation rates of $SO_2$ and $H_2S$ by OH are based on refs [53, 54] respectively. To account for the oxidation loss of OH to the initial high concentrations of $SO_2$ and $H_2S$ in the SAI plume, a parametrization is employed (see Supporting Information for details):

$$[OH] = [OH]^0 \times (1 + R_H^0)/(1 + R_H) \quad (5)$$

where $R_H$ is defined as

$$R_H = (k_{OH+O3}[O_3] + k_a[SO_2] + k_b[H_2S])/(k_{HO2+O3}[O_3] + k_{HO2+NO}[NO]) \quad (6)$$

In these equations, $[OH]^0$ is the ambient [OH], $R_H^0$ is the ratio of $[HO_2]$ to [OH] in the absence of $SO_2$ and $H_2S$ oxidation. $k_{OH+SO2}$, $k_{OH+H2S}$, $k_{OH+O3}$, $k_{HO2+O3}$, and $k_{HO2+NO}$ are reaction rates given in Supporting Information. $[O_3]$ and [NO] are the concentrations of $O_3$ and NO.

In this study, the baseline values for T, RH, Q, and $[O_3]$ are derived from GEOS-Chem annual averages for the tropical site and spring (MAM) for the subpolar site, with monthly means used for seasonal sensitivity analyses. Diurnal variations of T, RH, Q, and $[O_3]$ at the two sites are minimal and thus are not explicitly considered. The annual, spring, or monthly mean diurnal variations of [OH] and [NO] are employed.

The initial OH depletion described above (eq 5) is important, especially for $H_2S$ SAI, but it does not change the main conclusions of this study (Figures S2−S3). The degree of depletion depends on $[SO_2]$ and/or $[H_2S]$ and, therefore, on the injection rates. For the baseline cases, the depletion significantly decreases [OH] in the plume during the first several days for $SO_2$ SAI and during the first 5−10 days for $H_2S$ SAI. For baseline $SO_2$ SAI, this initial OH depletion reduces $FM_{nucl}$ from 36.5% to 33.1% and from 53.0% to 49.3% at tropical and subpolar sites, respectively. For baseline $H_2S$ SAI, this initial OH depletion reduces $FM_{nucl}$ from 38.6% to 30.7% and from 52.4% to 40.1% at tropical and subpolar sites, respectively. These substantial differences, particularly for $H_2S$ SAI, highlight the need to account for OH depletion in initial plumes with high $[SO_2]$ and/or $[H_2S]$. The present study provides a simplified parametrization of the OH depletion and a more comprehensive treatment of photochemistry may help reduce this uncertainty.

### M4: Baseline and Sensitivity Study Cases

This study employs the model outlined in M1 to analyze particle formation and evolution in $H_2S$ and $SO_2$ SAI plumes at two sites across different seasons and conditions. The parameters for baseline and sensitivity analyses are summarized in Table 1. The baseline values and sensitivity study range for MIR and $\gamma$ are as described in M2. Background particles are assumed to have log-normal distributions with a median dry diameter of 0.5 $\mu$m and a standard deviation of 2.0 estimated from global model simulations,[21] with concentrations depending on the specified surface area ($S_B$). Without volcanic activity, $S_B$ at approximately 3 km above the tropopause varies from about 1 $\mu m^2/cm^3$ in tropical regions to about 3 $\mu m^2/cm^3$ in polar regions. As pointed out earlier, SAI can significantly increase $S_B$. In the lower stratosphere, the oxidation lifetime of $H_2S$ is on the order of days, whereas $SO_2$ persists for weeks or longer. Ambient $SO_2$ levels outside plumes are typically low, around 1 ppt in tropical regions and up to 5−10 ppt in polar regions, but can exceed 1000 ppt in areas with ongoing SAI. The baseline assumptions set $S_B$ at 5 $\mu m^2/cm^3$ and ambient $SO_2$ at 100 ppt, with sensitivity ranges extending to 30 $\mu m^2/cm^3$ and 1000 ppt, respectively, to simulate conditions with enhanced aerosol and $SO_2$ layers associated with $SO_2$ or $H_2S$ SAI.

As discussed in M3, [OH] has strong seasonal and diurnal variations. We use annually mean [OH] diurnal variations for baseline case and monthly mean of individual months (Jan−Dec) for sensitivity study. Our test indicates that the results are not sensitive to injection local time (not shown), and we use 00:00 as injection time in all simulations. For injection altitudes or heights, 3 km above tropopause is used as baseline value and sensitivity study covers 1−11 km above tropopause.

Particle formation is a critical process influencing SAI effectiveness, as it determines the size distribution evolution. The oxidation products of $H_2S$ and $SO_2$ (primarily $H_2SO_4$) can either nucleate to form new particles or condense onto existing particles. The partitioning depends heavily on nucleation mechanisms. The baseline scheme uses BIMN and a sensitivity analysis considers KBHN to evaluate the role of ionization.[37] BIMN reduces to KBHN when ionization rates are zero, allowing assessment of ionization effects, especially given the spatial variability of ionization rates in the lower stratosphere (Figure 1c). This approach provides insights into the influence of ionization on particle nucleation and growth in the context of SAI.

## ■ ASSOCIATED CONTENT

### Data Availability Statement

Data shown in the paper are available in the data repository at https://zenodo.org/records/24238098. **Code availability:** The GEOS-Chem model employed to obtain atmospheric conditions used in this study is available at the GEOS-Chem "Science Codebase" repository (https://github.com/geoschem/geos-chem). The lookup tables (and code) for BIMN and KBHN can be accessed via the Zenodo data repository (10.5281/zenodo.3483797).

### Supporting Information

The Supporting Information is available free of charge at https://pubs.acs.org/doi/10.1021/acs.est.6c06576.

Hydroxyl radical (OH) concentration in the lower stratosphere and SAI plume; 30-day time evolution of selected variables and particle size distributions in exhaust plumes with $SO_2$ and $H_2S$ SAI at the subpolar site;

Downloaded from pubs.acs.org/esthag/article-pdf/doi/10.1021/acs.est.6c06576/6928922O/acs.est.6c06576.pdf by guest on 28 November 2026



https://doi.org/10.1021/acs.est.6c06576
Environ. Sci. Technol. XXXX, XXX, XXX−XXX

impacts of initial OH depletion at the tropical and subpolar sites (PDF)

## AUTHOR INFORMATION

### Corresponding Author

**Fangqun Yu** − *Atmospheric Sciences Research Center, University at Albany, State University of New York, Albany, New York 12226, United States;* orcid.org/0000-0001-8862-4835; Email: fyu@albany.edu

Complete contact information is available at: https://pubs.acs.org/10.1021/acs.est.6c06576

### Author Contributions

F.Y. designed and carried out the study and wrote the manuscript.

### Notes

The author declares no competing financial interest.

## ACKNOWLEDGMENTS

This research has been supported by SilverLining and NSF (AGS-2325458). The author thanks three anonymous reviewers for suggestions to improve the manuscript.

## REFERENCES

(1) Hansen, J. E.; Kharecha, P.; Sato, M.; Tselioudis, G.; Kelly, J.; Bauer, S. E.; Ruedy, R.; Jeong, E.; Jin, Q.; Rignot, E.; Velicogna, I.; Schoeberl, M. R.; von Schuckmann, K.; Amponsem, J.; Cao, J.; Keskinen, A.; Li, J.; Pokela, A. Global Warming Has Accelerated: Are the United Nations and the Public Well-Informed? *Environ. Sci. Policy Sustain. Dev.* **2025**, *67* (1), 6−44.

(2) Foster, G.; Rahmstorf, S. Global warming has accelerated significantly. *Geophys. Res. Lett.* **2026**, *53*, No. e2025GL118804.

(3) Armstrong McKay, D. I.; Staal, A.; Abrams, J. F.; Winkelmann, R.; Sakschewski, B.; Loriani, S.; Fetzer, I.; Cornell, S. E.; Rockström, J.; Lenton, T. M. Exceeding 1.5 °C global warming could trigger multiple climate tipping points. *Science* **2022**, *377*, No. eabn7950.

(4) Ripple, W.; Wolf, C.; Rockstrom, J.; Richardson, K.; Wunderling, N.; Gregg, J. W.; Westerhold, T.; Schellnhuber, H. J. The risk of a hothouse Earth trajectory. *One Earth* **2026**, *9*, 101565.

(5) World Meteorological Organization(WMO). *Scientific Assessment of Ozone Depletion: 2022, Global Ozone Research and Monitoring Project*. WMO: Switzerland, 2022509.

(6) Intergovernmental Panel on Climate Change. *Climate Change 2021 − The Physical Science Basis*. Cambridge University Press: UK, 2023. DOI: 10.1017/9781009157896.

(7) Burke, M.; Zahid, M.; Diffenbaugh, N. S.; Hsiang, S. Quantifying climate loss and damage consistent with a social cost of carbon. *Nature* **2026**, *651*, 959−966.

(8) Keith, D. W. Geoengineering the climate: History and prospect. *Annu. Rev. Energy Environ.* **2000**, *25*, 245−284.

(9) Crutzen, P. Albedo Enhancement by Stratospheric Sulfur Injections: A Contribution to Resolve a Policy Dilemma? *Clim. Change* **2006**, *77*, 211−220.

(10) National Academies of Sciences. *Reflecting Sunlight: recommendations for Solar Geoengineering Research and Research Governance*; The National Academies Press: Washington, DC, 2021. DOI: 10.17226/25762

(11) Wanser, K.; Doherty, S. J.; Hurrell, J. W.; Wong, A. Near-term climate risks and sunlight reflection modification: a roadmap approach for physical sciences research. *Clim. Change* **2022**, *174* (3−4), 23.

(12) United Nations Environment Programme. *One Atmosphere: an Independent Expert Review On Solar Radiation Modification Research And Deployment*; UNEP: Nairobi, 2023.

(13) Haywood, J. M.; Boucher, O.; Lennard, C.; Storelvmo, T.; Tilmes, S.; Visioni, D. World Climate Research Programme lighthouse activity: an assessment of major research gaps in solar radiation modification research. *Front. Clim.* **2025**, *7*, 1507479.

(14) Robock, A.; Marquardt, A.; Kravitz, B.; Stenchikov, G. Benefits, risks, and costs of stratospheric geoengineering. *Geophys. Res. Lett.* **2009**, *36*, L19703.

(15) Robock, A. Volcanic eruptions and climate. *Rev. Geophys.* **2000**, *38*, 191−219.

(16) Pierce, J. R.; Weisenstein, D. K.; Heckendorn, P.; Peter, T.; Keith, D. W. Efficient formation of stratospheric aerosol for climate engineering by emission of condensible vapor from aircraft. *Geophys. Res. Lett.* **2010**, *37* (18), L18805.

(17) Franke, J.; Smith, W.; Slavens, A.; Keutsch, F. N.; Yu, F.; Keith, D. Tradeoffs between sulfuric acid aerosol precursors for stratospheric aerosol geoengineering. *Environ. Sci. Technol.* **2026**, *60* (26), 18555−18562.

(18) Kravitz, B.; Robock, A.; Boucher, O.; Schmidt, H.; Taylor, K. E.; Stenchikov, G.; Schulz, M. The Geoengineering Model Intercomparison Project (GeoMIP). *Atmos. Sci. Lett.* **2011**, *12* (2), 162−167.

(19) Tilmes, S.; Richter, J. H.; Kravitz, B.; Macmartin, D. G.; Mills, M. J.; Simpson, I. R.; Glanville, A. S.; Fasullo, J. T.; Phillips, A. S.; Lamarque, J. F.; Tribbia, J.; Edwards, J.; Mickelson, S.; Ghosh, S. CESM1(WACCM) stratospheric aerosol geoengineering large ensemble project. *B. Am. Meteorol. Soc.* **2018**, *99*, 2361−2371.

(20) Richter, J. H.; Visioni, D.; MacMartin, D. G.; Bailey, D. A.; Rosenbloom, N.; Dobbins, B.; Lee, W. R.; Tye, M.; Lamarque, J.-F. Assessing Responses and Impacts of Solar climate intervention on the Earth system with stratospheric aerosol injection (ARISE-SAI): protocol and initial results from the first simulations. *Geosci. Model Dev.* **2022**, *15*, 8221−8243.

(21) Yu, F.; Luo, G.; Nair, A. Higher efficacy of $SO_2$ and $H_2SO_4$ Stratospheric Aerosol Injection: Insights from CESM2 and GEOS-Chem with Advanced Particle Microphysics (APM). *Environ. Res. Lett.* **2026**, *21*, 044006.

(22) Fritz, T. M.; Eastham, S. D.; Speth, R. L.; Barrett, S. R. H. The role of plume-scale processes in long-term impacts of aircraft emissions. *Atmos. Chem. Phys.* **2020**, *20*, 5697−5727.

(23) Sun, H.; Eastham, S.; Keith, D. Developing a Plume-in-Grid model for plume evolution in the stratosphere. *J. Adv. Model. Earth Syst.* **2022**, *14*, No. e2021MS002816.

(24) Rasch, P. J.; Tilmes, S.; Turco, R. P.; Robock, A.; Oman, L.; Chen, C.-C.(.; Stenchikov, G. L.; Garcia, R. R. An overview of geoengineering of climate using stratospheric sulphate aerosols. *Philos. Trans. R. Soc. A* **2008**, *366* (1882), 4007−4037.

(25) Eastham, S. D.; Butler, A. H.; Doherty, S. J.; Gasparini, B.; Tilmes, S.; Bednarz, E. M.; et al. Key gaps in models' physical representation of climate intervention and its impacts. *J. Adv. Model. Earth Syst.* **2025**, *17*, No. e2024MS004872.

(26) Reflective Scientific Advisory Board: *2024 Meeting Report*, 2025; Reflective https://reflectiveclimate.substack.com/p/reflective-scientific-advisory-board.

(27) Benduhn, F.; Schallock, J.; Lawrence, M. G. Early growth dynamical implications for the steerability of stratospheric solar radiation management via sulfur aerosol particles. *Geophys. Res. Lett.* **2016**, *43* (18), 9956−9963.

(28) Yu, F.; Anderson, B.; Pierce, J.; Wong, A.; Nair, A.; Luo, G.; Herb, J. On nucleation pathways and particle size distribution evolutions in stratospheric aircraft exhaust plumes with $H_2SO_4$ enhancement. *Environ. Sci. Technol.* **2024**, *58*, 6934.

(29) Yu, F.; Turco, R. P. The role of ions in the formation and evolution of particles in aircraft plumes. *Geophys. Res. Lett.* **1997**, *24* (15), 1927−1930.

(30) Yu, F. *A Study Of The Formation And Evolution Of Aerosols And Contrails In Aircraft Wakes: Development, Validation And Application Of An Advanced Particle Microphysics (APM) Model*. Doctoral Dissertation, University of California, Los Angeles (UCLA), Los Angeles; 1998 p.183.

Downloaded from pubs.acs.org/esthag/article-pdf/doi/10.1021/acs.est.6c06576/6928220/acs.est.6c06576.pdf by guest on 28 November 2026

(31) Voigt, C.; Märkl, R.; Sauer, D.; Dischl, R.; Renard, C.; Seeliger, K.; Yu, F.; Kaufmann, S.; Bräuer, T.; Jurkat-Witschas, T.; et al. Substantial aircraft contrail formation at low soot emission levels. *Nature* **2026**, *652* (8108), 112−118.
(32) Jackson, L. S.; Crook, J. A.; Jarvis, A.; Leedal, D.; Ridgwell, A.; Vaughan, N.; Forster, P. M. Assessing the controllability of Arctic sea ice extent by sulfate aerosol geoengineering. *Geophys. Res. Lett.* **2015**, *42* (4), 1223−1231.
(33) Lee, W. R.; MacMartin, D. G.; Visioni, D.; Kravitz, B. High-latitude stratospheric aerosol geoengineering can be more effective if injection is limited to spring. *Geophys. Res. Lett.* **2021**, *48*, No. e2021GL092696.
(34) Smith, W.; Bartels, M. F.; Boers, J. G.; Rice, C. V. On thin ice: Solar geoengineering to manage tipping element risks in the cryosphere by 2040. *Earth's Future* **2024**, *12* (8), No. e2024EF004797.
(35) Duffey, A.; Henry, M.; Smith, W.; Tsamados, M.; Irvine, P. J. Low-Altitude High-Latitude Stratospheric Aerosol Injection Is Feasible With Existing Aircraft. *Earth's Future* **2025**, *13* (4), No. e2024EF005567.
(36) Duffey, A.; Lee, W.; Wheeler, L.; Irvine, P.; Wagman, B.; Henry, M.; Visioni, D.; Tsamados, M.; MacMartin, D. The global climate response to High-Latitude Low-Altitude Stratospheric Aerosol Injection (HiLLA-SAI). *Earth Syst. Dynam.* **2026**, *17*, 353−385.
(37) Yu, F.; Luo, G.; Nair, A. A.; Eastham, S.; Williamson, C. J.; Kupc, A.; Brock, C. A. Particle number concentrations and size distributions in the stratosphere: implications of nucleation mechanisms and particle microphysics. *Atmos. Chem. Phys.* **2023**, *23*, 1863−1877.
(38) Kirkby, J.; Curtius, J.; Almeida, J.; Dunne, E.; Duplissy, J.; Ehrhart, S.; Franchin, A.; Gagné, S.; Ickes, L.; Kürten, A.; et al. The role of sulfuric acid, ammonia and galactic cosmic rays in atmospheric aerosol nucleation. *Nature* **2011**, *476*, 429−433.
(39) Dunne, E. M.; Gordon, H.; Kürten, A.; Almeida, J.; Duplissy, J.; Williamson, C.; Ortega, I. K.; Pringle, K. J.; Adamov, A.; Baltensperger, U.; et al. Global atmospheric particle formation from CERN CLOUD measurements. *Science* **2016**, *354* (6316), 1119−1124.
(40) Williamson, C. J.; Kupc, A.; Axisa, D.; Bilsback, K. R.; Bui, T.; Campuzano-Jost, P.; Dollner, M.; Froyd, K. D.; Hodshire, A. L.; Jimenez, J. L.; Kodros, J. K.; Luo, G.; Murphy, D. M.; Nault, B. A.; Ray, E. A.; Weinzierl, B.; Wilson, J. C.; Yu, F. Q.; Yu, P. F.; Pierce, J. R.; Brock, C. A. A large source of cloud condensation nuclei from new particle formation in the tropics. *Nature* **2019**, *574*, 399−403.
(41) Turco, R. P.; Hamill, P.; Toon, O. B.; Whitten, R. C.; Kiang, C. S. A one-dimensional model describing aerosol formation and evolution in the stratosphere, Part I, Physical processes and mathematical analogs. *J. Atmos Sci.* **1979**, *36*, 699−717.
(42) Jacobson, M. Z.; Turco, R. P. Simulating condensational growth, evaporation and coagulation of aerosols using a combined moving and stationary size grid. *Aerosol Sci. Technol.* **1995**, *22*, 73−92.
(43) McClellan, J.; Keith, D. W.; Apt, J. Cost analysis of stratospheric albedo modification delivery systems *Environ. Res. Lett.* **2012**, *7*, 034019.
(44) Smith, W.; Wagner, G. Stratospheric aerosol injection tactics and costs in the first 15 Years of deployment. *Environ. Res. Lett.* **2018**, *13* (12), 124001.
(45) Bingaman, D. C.; Rice, C. V.; Smith, W.; Vogel, P. A Stratospheric Aerosol Injection Lofter Aircraft Concept: Brimstone Angel. In.*AIAA 2020−0618, AIAA Scitech 2020 Forum*.American Institute of Aeronautics and Astronautics; 2020. p. 0618. DOI: DOI: 10.2514/6.2020-0618.
(46) Smith, W. The cost of stratospheric aerosol injection through 2100. *Environ. Res. Lett.* **2020**, *15*, 114004.
(47) Schripp, T.; Anderson, B.; Crosbie, E. C.; Moore, R. H.; Herrmann, F.; Oßwald, P.; Wahl, C.; Kapernaum, M.; Köhler, M.; Le Clercq, P.; et al. Impact of Alternative Jet Fuels on Engine Exhaust Composition during the 2015 ECLIF Ground-Based Measurements Campaign. *Environ. Sci. Technol.* **2018**, *52*, 4969−4978.
(48) Schumann, U.; Schlager, H.; Arnold, F.; Baumann, R.; Haschberger, P.; Klemm, O. Dilution of aircraft exhaust plumes at cruise altitudes. *Atmos. Environ.* **1998**, *32* (18), 3097−3103.
(49) Dürbeck, T.; Gerz, T. Dispersion of aircraft exhausts in the free atmosphere. *J. Geophys. Res.: Atmos.* **1996**, *101* (D20), 26007−26015.
(50) Bey, I.; Jacob, D. J.; Yantosca, R. M.; Logan, J. A.; Field, B. D.; Fiore, A. M.; Li, Q.; Liu, H. Y.; Mickley, L. J.; Schultz, M. G. Global modeling of tropospheric chemistry with assimilated meteorology: Model description and evaluation. *J. Geophys. Res.: Atmos.* **2001**, *106*, 23073−23095.
(51) Eastham, S. D.; Weisenstein, D. K.; Barrett, S. R. Development and evaluation of the unified tropospheric−stratospheric chemistry extension (UCX) for the global chemistry-transport model GEOS-Chem. *Atmos. Environ.* **2014**, *89*, 52−63.
(52) Hanisco, T. F.; Lanzendorf, E. J.; Wennberg, P. O.; Perkins, K. K.; Stimpfle, R. M.; Voss, P. B.; Anderson, J. G.; Cohen, R. C.; Fahey, D. W.; Gao, R. S.; Hintsa, E. J.; Salawitch, R. J.; Margitan, J. J.; McElroy, C. T.; Midwinter, C. Sources, Sinks, and the Distribution of OH in the Lower Stratosphere. *J. Phys. Chem. A* **2001**, *105*, 1543−1553.
(53) Bates, K. H.; Evans, M. J.; Henderson, B. H.; Jacob, D. J. Impacts of updated reaction kinetics on the global GEOS-Chem simulation of atmospheric chemistry. *Geosci. Model Dev.* **2024**, *17*, 1511−1524.
(54) Mueller, S. F.; Mao, Q.; Mallard, J. W. Modeling natural emissions in the Community Multiscale Air Quality (CMAQ) model − Part 2: Modifications for simulating natural emissions. *Atmos. Chem. Phys.* **2011**, *11*, 293−320.

Downloaded from pubs.acs.org/esthag/article-pdf/doi/10.1021/acs.est.6c06576/6289220/acs.est.6c06576.pdf by guest on 28 November 2026


https://doi.org/10.1021/acs.est.6c06576
*Environ. Sci. Technol.* XXXX, XXX, XXX−XXX